Journal of Applied Sciences and Nanotechnology

Journal homepage: jasn.uotechnology.edu.iq

Synthesis and Characterization of Perovskite $Na_{0.5}Bi_{0.5}Ti_{0.94}Fe_{0.06}O_{2.97}$ Film for Photovoltaic Applications

Husam Nahedh*, Odai N. Salman, Mukhlis M. Ismail

Department of Applied Sciences, University of Technology - Iraq

ARTICLE INFO

Article history:
Received: January, 11, 2024
Accepted: April, 20, 2024
Available online: June, 10, 2024

Keywords:
NBTF nanostructure,
Perovskite,
Oxygen vacancies,
Electrical conductivity,
Photodiode

Corresponding Author:
H. Nahedh
husamnahidh@yahoo.com

ABSTRACT

In this study, sodium bismuth titanate ferroelectric ceramics with a nanoscale structure and low iron content (NBTF) were prepared, providing an alternative to lead-based materials. Lead poses environmental and health risks due to its toxicity. NBTF aims to develop a more sustainable ferroelectric composition. The structural, optical, and electrical properties of $Na_{0.5}Bi_{0.5}Ti_{1-x}Fe_xO_{3-0.5x}$ (x=0.06) were investigated. X-ray diffraction revealed the material crystallizes in the rhombohedral phase, with crystallite size of approximately 19.1 nm in size. Infrared and Raman spectroscopy confirmed the formation of a perovskite structure containing Fe ions, evidenced by Ti-O stretching and O-Fe-O bending vibrations. Raman spectroscopy also identified a broad peak at high frequencies, suggesting the generation of oxygen vacancies induced by the dopant. Electrical characterization demonstrated semiconductor behavior with a bandgap of 1.84 eV, showing potential for optoelectronic applications. The study focused on the effect of oxygen vacancies on electrical conductivity. Furthermore, a nano-perovskite heterojunction photodiode comprising Al/p-Si/NBTF/Ag was successfully fabricated and evaluated. Under reverse bias, photocurrent increased compared to the dark state with rising illumination intensity. Device parameters including reaction order, ideality factor, and carrier lifetime were calculated. Collectively, these results indicate promise for integrating this heterostructure photodiode into electronic circuitry applications.

https://doi.org/10.53293/jasn.2024.7238.1269, Department of Applied Sciences, University of Technology - Iraq.
© 2024 The Author(s). This is an open access article under the CC BY license (http://creativecommons.org/licenses/by/4.0/).

1. Introduction

Oxygen vacancies in lead-free ceramic sodium bismuth titanate ($Na_{0.5}Bi_{0.5}TiO_3$, NBT) are caused by nonstoichiometric bismuth or acceptor doping. In ferroelectric ceramics, the defects formed, such as oxygen vacancies are not mobile compared to the NBT, where acceptor doping and oxygen vacancies may give rise to a surprising ionic conductivity [1, 2]. The significant increase in conductivity of piezoelectric materials under non-stoichiometry is very detrimental as the defective chemical properties of lead-based ferroelectrics such as lead zirconate titanate (PZT) cannot be exploited in those lead-free compounds [3, 4].

There are two main factors in preparing the NBT, the first is the concentration of doping and the second is the concentration of oxygen vacancies [5–8]. It has been observed that the mobility of oxygen vacancies exhibits a nonlinear behavior, through which the ionic conductivity changes significantly depending on these small additions in the acceptor concentration.

In recent years, many researchers have attracted interest in studying ferroelectric perovskite materials for photovoltaic applications because of their excellent structural stability and the abundance of materials that consist of their composition [9]. It has been reported that some ferroelectric perovskite oxides have been applied in photovoltaic applications, such as $BaTiO_3$ [10], $BiFeO_3$ [11], and $BaSnO_3$ [12]. One of the most potential sustainable perovskite oxide systems to substitute lead-based ceramics is NBT ceramics, which display a high conductivity, a high polarization of 38 $\mu C/cm^2$, and a high Curie temperature of about 320°C [13].

Some differences in the properties of NBT may occur due to structural changes and phase transformations caused by changing the temperature or applying an external electric field. Combining NBT with other compounds as solid solutions, such as (1-x)($Na_{0.5}Bi_{0.5}TiO_3$–(x)$Bi_{0.5}K_{0.5}TiO_3$ [14], or doping with other elements is considered the most prominent means focused on improving NBT perovskite properties [15].

In this work, NBT NPs were prepared using the hydrothermal route, and the optical, structural, and electrical characterization was studied. The low-cost nano Al/p-Si/NBTF/Ag heterojunction diode was fabricated. The current-voltage characteristics of heterojunctions were studied under dark and illumination conditions and the effect of the increase in illumination intensity on the Al/p-Si/NBTF/Ag diode under reverse bias conditions. Also, the V_{oc} decay as a function of time was analyzed.

2. Experimental details

Ferroelectric of $Na_{0.5}Bi_{0.5}Ti_{1-x}FexO_{3-0.5x}$ (x=0.06) were synthesized via the hydrothermal route. The primary components used in this work were TiO_2, $Bi(NO_3)_3.5H_2O$, $Fe(NO_3)_3.9H_2O$, and NaOH. The stoichiometric molar ratio of TiO_2 and $Bi(NO_3)_3.5H_2O$ was done to be 2:1 and was mixed under a magnetic stirrer for 20 min. After that, 18 M NaOH was added gradually to the stoichiometric solution and stirred until a homogenous solution form was obtained. Iron (III) nitrate nonahydrate was added to the combination and stirred for 20 min. The chemical combination was placed inside 60% of the total capacity of a stainless-steel autoclave lined with Teflon and then heated to 200 °C for 36 hours. The product was centrifuged several times with deionized water until (pH~7). At last, the powder was dried in an oven at 100 °C. The preparation method diagram for NBTF NPs was displayed, as shown in Fig. 1.

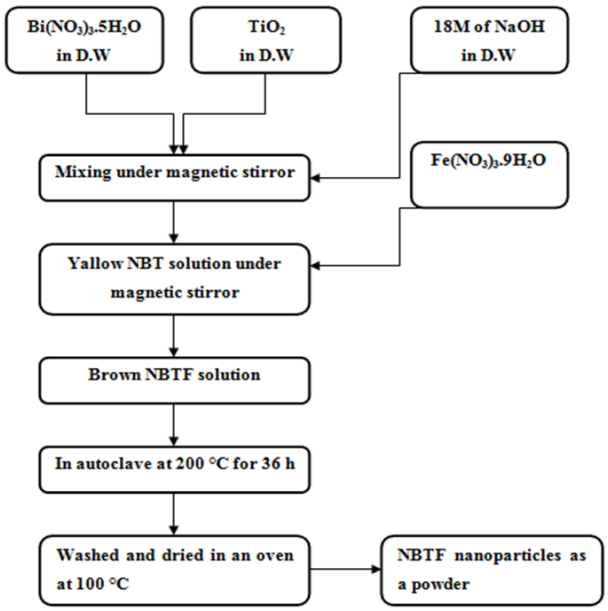

Figure 1: Flow diagram of the hydrothermal method for synthesizing NBTF powder.

For electrical measurement, the $Na_{0.5}Bi_{0.5}Ti_{0.94}Fe_{0.06}O_{2.97}$ (NBTF) thin film was deposited on the fluorine tin oxide FTO substrate by the spin coating method at 3500 rpm for 2 min. To achieve the required thickness, the depositing procedure was repeated several times. The film was exposed to an annealing process at 150 °C for ten minutes. Using a thermal evaporation technique, Aluminum (Al) electrodes were deposited on the film.

Al metal was evaporated on the back side of the P-SI as the ohmic contact for photovoltaic applications. The NBTF was deposited on the mirror-polished side of Al/P-Si, and then silver paste was used as an electrode to complete the construction of the photodiode device, as shown in Fig. 2.

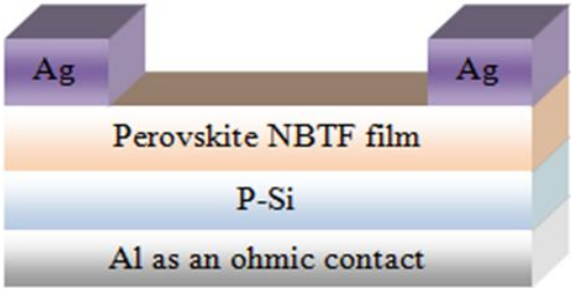

Figure 2: schematic diagram of Al/p-Si/NBTF/Ag photodiode device

3. Results and discussion

Fig. 3 displays the XRD pattern of the iron-doped sodium bismuth titanate prepared by a hydrothermal process at 200 °C for 36 hours. The crystalline phases of NBTF thin film were obtained, and there appeared to be no indication of any phases besides NBT phases (JCPDS NO. 36-0340). The reflection of the (110), (101), (012), (220), and (123) planes of the rhombohedral NBTF thin film were attributed to the diffraction peaks at (2θ) values of 22.68°, 32.28°, 39.92°, 46.52°, and 57.76°, 50.50°, respectively. The diffraction peaks broadening is linked to the nanostructure of the compound. The position of all reflections is attributed to the R3c space group.

The average crystallite size (D) of NBTF thin film was calculated using the Scherrer formula as in **Eq. (1)** [16] and estimated to be about 19.1 nm.

$$\boldsymbol{D = \frac{K\lambda}{\beta cos\theta}} \qquad (1)$$

Where β is full width at half maximum FWHM and k is constant.

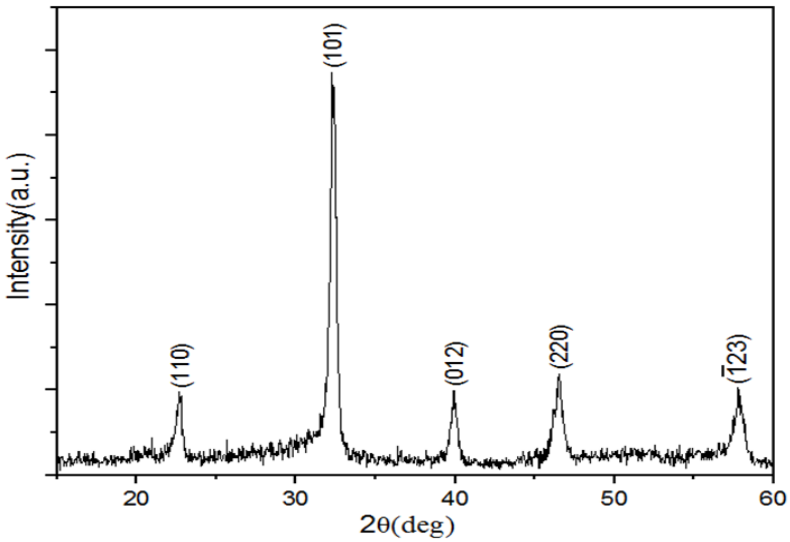

Figure 3: XRD analysis of NBTF thin film.

On the other hand, the average crystalline size of the perovskite NBTF thin film was found to be 33.27 nm using the Williamson-Hall method as the following **Eq. (2)** [17]:

$$\boldsymbol{\beta cos\theta = \mathcal{E}(4sin\theta) + \frac{k\lambda}{D}} \qquad (2)$$

By plotting a straight line between $\beta cos\theta$ and $4sin\theta$ as shown in Fig. 4, we can obtain the average crystallite size by calculating the intercept (DW.H= kλ/c), where c represents the intercept.

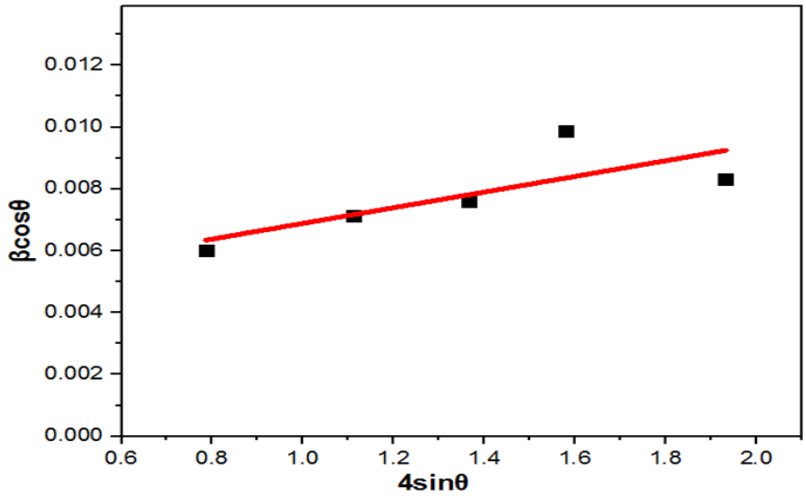

Figure 4: Williamson Hall Plot for NBTF thin film.

Fig. 5 shows the FTIR spectrum of $Na_{0.5}Bi_{0.5}Ti_{0.94}Fe_{0.06}O_{2.97}$ nanostructure. FTIR spectra were obtained at room temperature, and the wave number range was between 400 cm^{-1} and 4000 cm^{-1} using the KBr pellets approach. The bandwidth seen at around 3413 cm^{-1} is related to the vibrational pattern caused by stretching O-H bonds. The two low-intensity bands at 2850 cm^{-1} and 2924 cm^{-1} were identified due to vibrational B-O bonds [18]. The vibration of the H-O-H bond causes the band at 1604 cm^{-1} as a result of water molecule absorption [19]. The band detects the N-O stretching mode of the nitro compound at 1427 cm^{-1}. The formation of the perovskite structure is confirmed by the appearance of a sharp band around 626 cm^{-1}, which is attributed to the vibration of the Ti-O stretching vibration. The band is situated at 420 cm^{-1}, corresponding to the O-Fe-O's bending vibration, representing the metal oxide modes in the perovskite structure [20, 21].

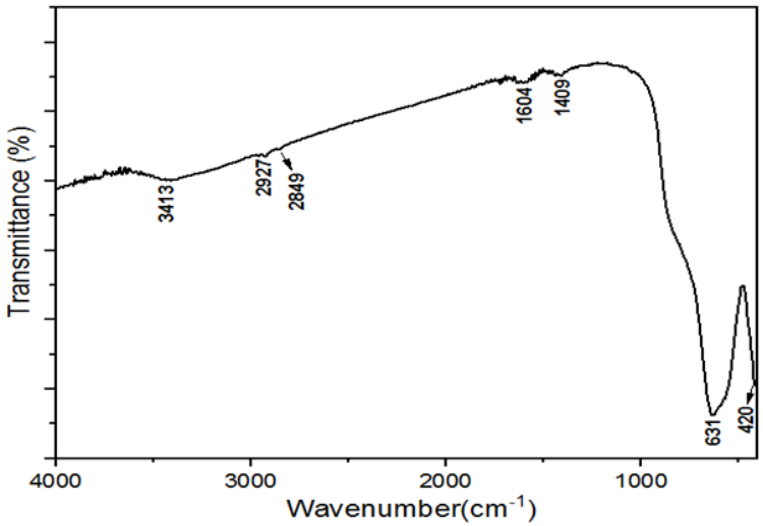

Figure 5: FTIR spectrum of NBTF.

The photoluminescence spectrum (PL) of $Na_{0.5}Bi_{0.5}Ti_{0.94}Fe_{0.06}O_{2.97}$ was excited by 323 nm at room temperature as shown in Fig. 6. The emission peak was observed and located in the red-light emission regions at 714 nm. The appearance of the peak in the high PL region around 714 nm is due to the formation of further oxygen vacancies caused by doping Fe ions in B-site of $Na_{0.5}Bi_{0.5}TiO_3$ [22, 23]. The energy gap of NBTF film was calculated by PL analysis to be 1.73 eV.

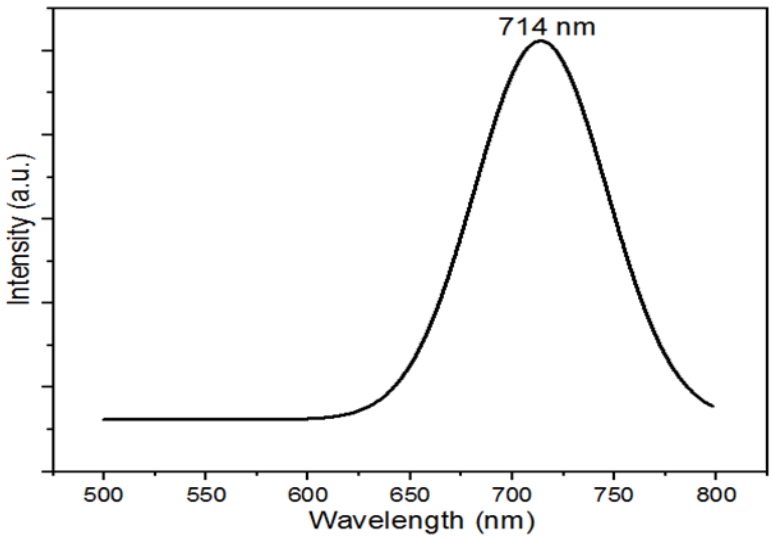

Figure 6: PL spectrum of NBTF thin film.

Fig. 7 displays the Raman spectrum of NBTF thin film in the frequency range 50-1200 cm^{-1}. Origin Pro employs the Lorentz function to fit the Raman active modes of NBTF thin film. The Raman modes of NBTF thin film consist of five prominent peaks. The NBT-based Raman modes at high frequencies, which are above approximately 700 cm^{-1}, are attributed to displacements of oxygen [24]. At the mid-frequencies, the two vibrational bands observed near 280 cm^{-1} and 550 cm^{-1} are ascribed to the Ti-O and TiO_6 octahedral, respectively [25]. The Bi-O and Na-O bonds represent the low frequencies, which are observable at around 77 cm^{-1} and 120 cm^{-1}, respectively [26, 27].

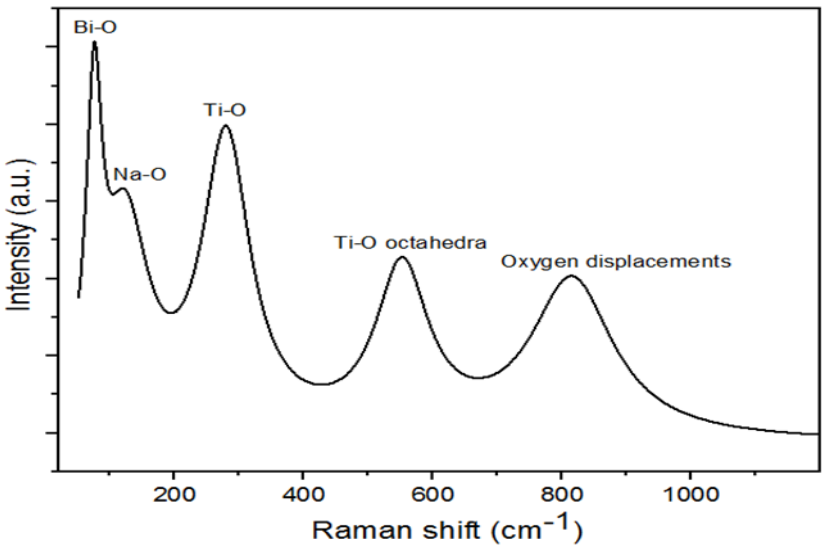

Figure 7: Raman spectrum of NBTF thin film.

Fig. 8a shows the UV.VIS spectrum of NBTF thin film. A significant absorption edge was observed around 570 nm and peaked at 520 nm, suggesting the incorporation of Fe ions in the host NBT crystal. Furthermore, an

absorbance peak appeared within the wavelength range of 700–800 nm, which may be attributed to the formation of localized states of the Fe ions [28]. The energy gap value of the NBTF thin film was calculated by drawing $(\alpha h\nu)^2$ against photonic energy (eV), as displayed in Fig. 8b, where α is the absorbance coefficient, h is the Planck constant, and ν is the frequency. The energy gap of NBTF was found to be 1.84 eV. The value of the obtained energy gap by UV-Vis is observed to be close to that calculated from the PL analysis.

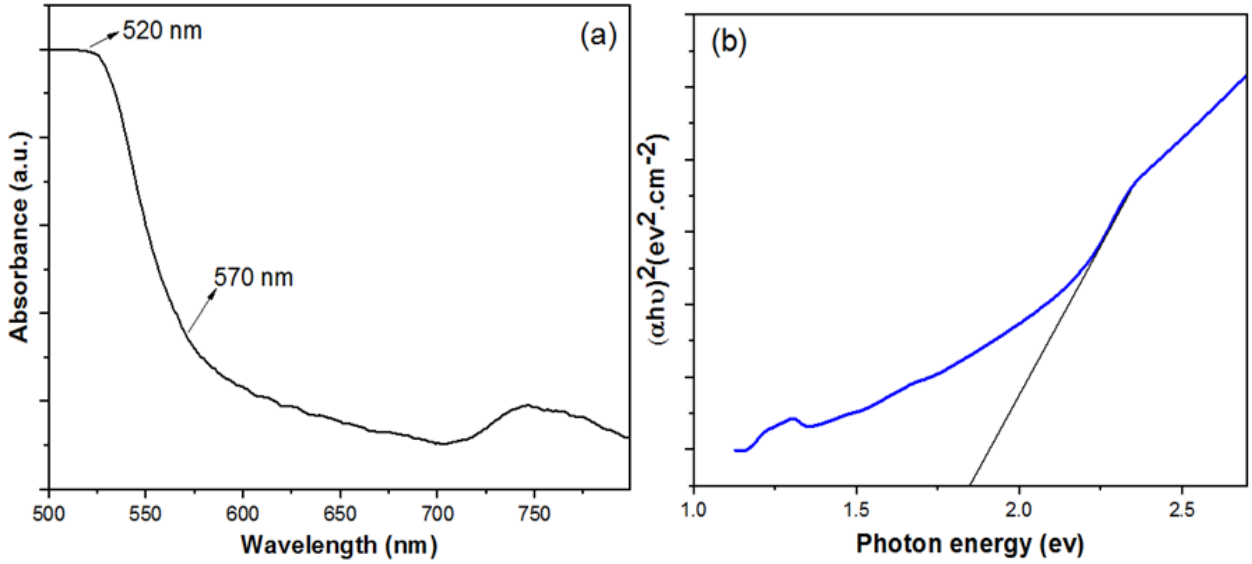

Figure 8: (a) UV.VIS spectrum (b) Energy bandgap NBTF thin film.

Fig. 9a shows that the surface morphology of the investigated NBTF thin film is densely packed and crystallized particles without any cracks, indicating that the prepared composition is polycrystalline. The cross-section of NBTF thin film (~ 350 nm) is shown in Fig. 9b.

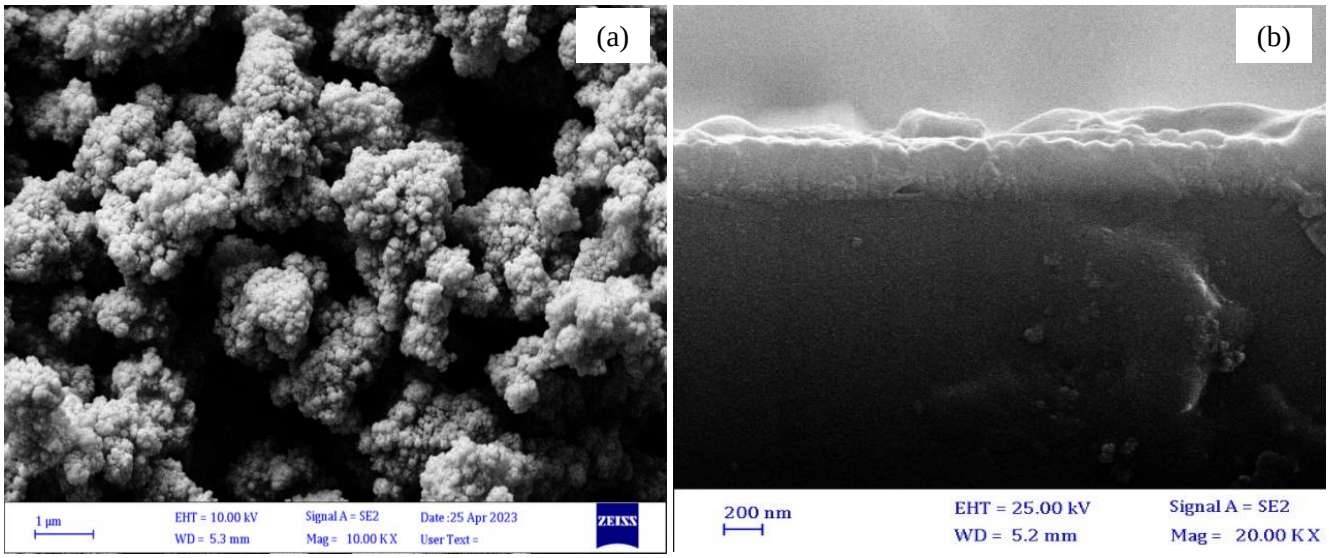

Figure 9: (a) FESEM image, (b) Cross section of NBTF thin film

The NBTF thin film has good DC electrical conductivity in the thermal range (303–453K), as shown in Fig. 10. The conductivity of the NBTF thin film behaves like that of a semiconductor, whereby the conductivity increases with rising temperature. The oxygen vacancies caused by adding a small amount of Fe enhance the conductivity of perovskite NBTF thin film. The NBTF thin film has two regions of an activation energy, which can be found

by plotting the slope between ln(σ) against 1000/T. The first and second activation energies were 0.008 and 0.0149 eV, respectively.

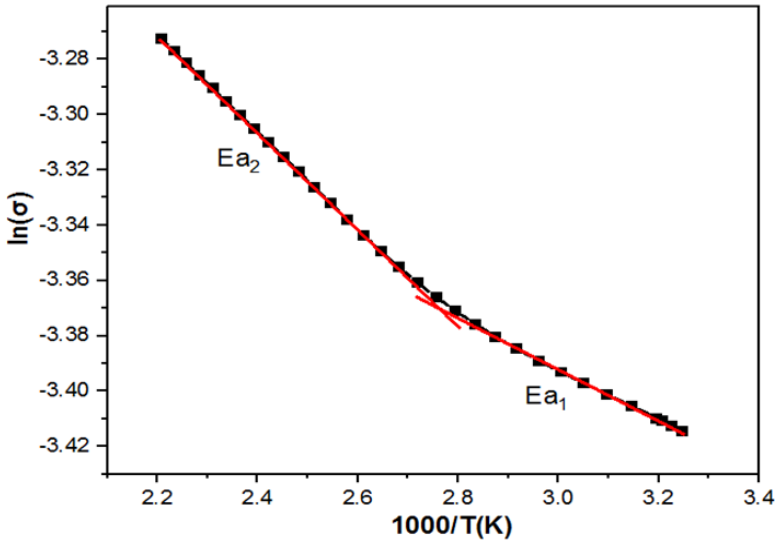

Figure 10: The DC electrical conductivity of NBTF thin film.

Fig. 11 displays the forward and reverse bias of the I-V curve of Al/p-Si/NBTFe/Ag heterojunction photodiode under dark and illuminated modes. Under dark conditions, the cut-in voltage was discovered to be 1 V, which reduces to 0.8 V under illumination. The current grows exponentially under forward bias because of the generation of additional electron-hole pairs, which contribute to the conduction process [29].

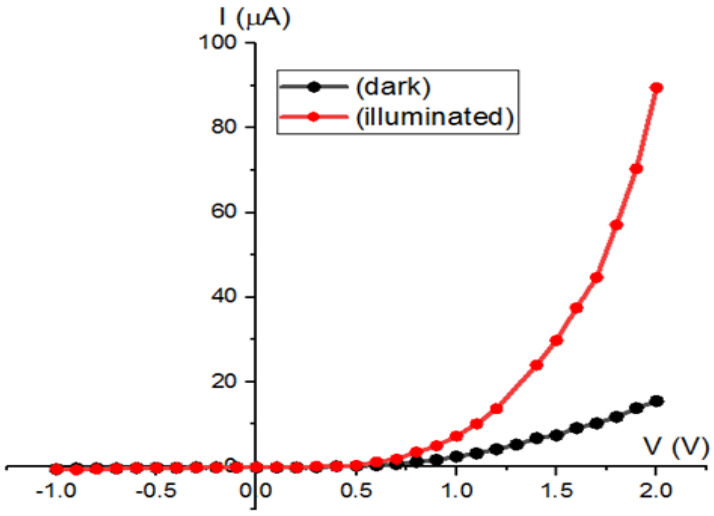

Figure 11: The (I-V) dark and illuminated (100 mW/cm^2) of Al/p-Si/NBTFe/Ag photodiode.

Fig. 12 shows the I_{ph}-V characteristics of Al/p-Si/NBTFe/Ag under 100 mW/cm^2 illumination with reverse bias voltage at different current densities from 35 to 100 mW/cm^2 and constant time. The current caused by illumination of Al/p-Si/NBTFe/Ag is higher than the dark current for reverse bias. Under illumination, the electron-hole pairs are photoinduced and generated in the heterojunction photodiode's depletion zone due to photon energy absorption (hv). In the reverse bias, it was observed that the photo-current increases with the increase of both the reverse bias voltage and light intensity because the photoexcited holes that move to p-Si can facilitate the separation of the electron-hole pairs. The forward current remained constant when the illumination intensity increased under

forward bias. This effect on forward bias is due to the inability of photoexcited electrons and holes to migrate towards the p-Si, which leads to difficulty in separating electron-hole pairs [30].

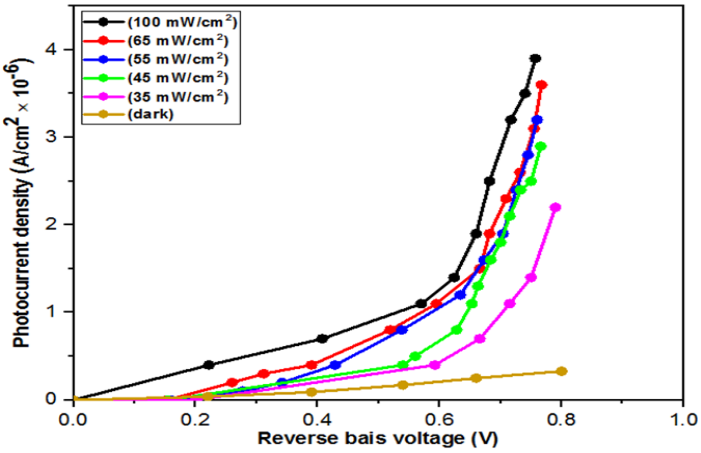

Figure 12: Photocurrent density vs reverse bias voltage of Al/p-Si/NBTFe/Ag photodiode under different illumination intensities.

The dependency of the photodiode's open circuit voltage on the light intensity's logarithmic is called the ideality factor (*n*) and studying the extent to which it deviates from the ideal behavior (*n*=1). In most cases, the diode exhibits non-ideal behavior (*n* > 1) due to the recombination of charge carriers. Fig. 13 exhibits the logarithmic illumination intensity dependent on the voltage open circuit (V_{oc}). The reaction order (β) and ideality factor (*n*) can be determined using the following **Eq. (3)** and **Eq. (4)** [31]:

$$\frac{dV_{oc}}{dlnI_O} = n\frac{KT}{q} \qquad (3)$$

$$\beta = \frac{1}{n} \qquad (4)$$

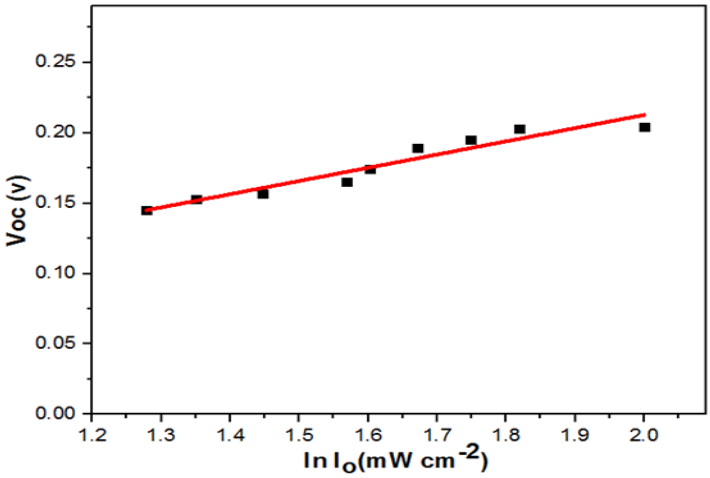

Figure 13: Semi-logarithmic diagram of the open-circuit voltage vs. Light intensity for Al/p-Si/NBTFe/Ag photodiode device.

The obtained values of *n* and β for the Al/p-Si/NBTFe/Ag photodiode are 3.082 and 0.33, respectively, referring to ideal photodiode behavior. The diode behavior is near ideal when the ideality factor is greater than unity, caused by the back interaction through the conduction band at relatively high illumination intensity [32, 33].The reduction

of n below unity can be ascribed to either the recombination of electrons and holes in the depletion zone or the augmentation of the diffusion current caused by the rise in the applied voltage. Generally, ideality factor values ranging from 1 to 2 indicate an overlap of recombination and diffusion currents, while ideality factors in excess of 2 point to recombination current dominate in photovoltaic devices [34].

The electron lifetime is the rate time that requires the photogenerated electron in the excited state of the conduction band to return to its ground state in the valence band after recombination with a hole. Fig. 14a exhibits the higher V_{oc} with the decay after switching down the illumination, showing the recombination kinetics of conduction-band electrons for the Al/p-Si/NBTFe/Ag photodiode. The carrier's lifetime (τ_n) was calculated from the V_{oc} decay curve by using the following **Eq. (5)** [35]:

$$\boldsymbol{\tau_n = -\frac{K_B T}{q}\left(\frac{dV_{oc}}{dt}\right)^{-1}} \qquad (5)$$

The carrier lifetime was (τ_n) was found to be 2.87 sec. Fig. 14b illustrates the logarithmic curve of the carrier lifetime as a function of open-circuit voltage.

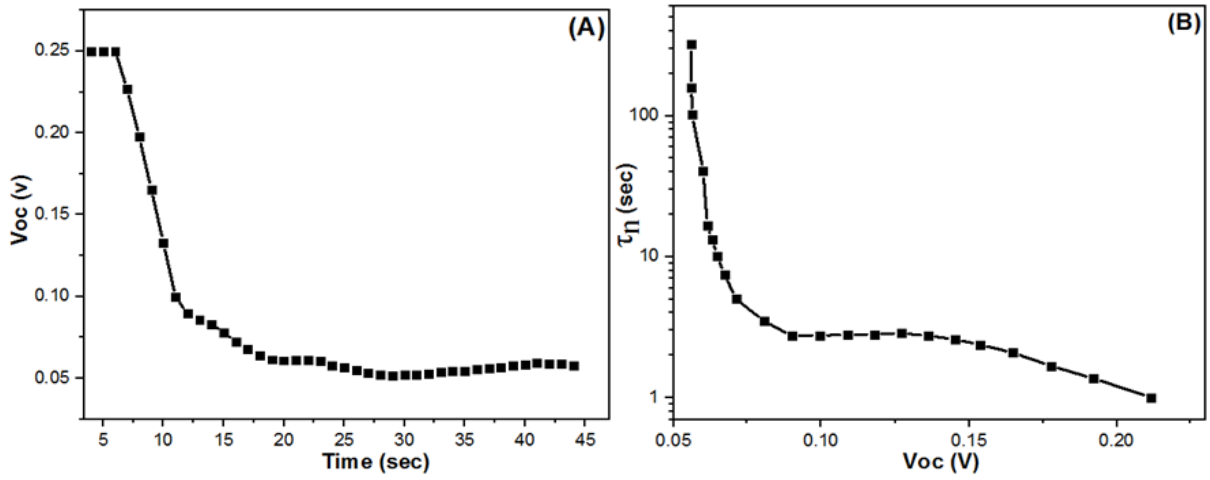

Figure 14: a) The decay of open-circuit voltage and, b) electron lifetime (τ_n) as a function of open-circuit voltage for Al/p-Si/NBTFe/Ag photodiode device.

4. Conclusions

In this study, the effect of adding 0.06 mol% Fe to the NBT host material on structural, optical, and electrical properties was investigated. XRD analysis confirmed the rhombohedral crystallite phase of NBTF with a crystallite size of approximately 19.1 nm. The presence of Ti-O and O-Fe-O functional groups as identified by infrared and Raman spectroscopy indicates the successful doping of Fe into the perovskite structure. The NBTF exhibited semiconductor behavior with a bandgap of ~1.84 eV, attributed to oxygen vacancies generated by the dopant. Relatively high DC conductivity was observed, as were two activation energies for the NBTF film. Under forward bias illumination from a xenon lamp, the NBTF photodiode current increased compared to the dark state. Notably, photocurrent also rose with higher reverse bias illumination intensity from the power supply. These findings demonstrate the potential of this heterojunction photodiode for integration into electronic circuit applications.

Conflict of Interest

The authors declare that they have no conflict of interest.

References

[1] G. Arlt and H. Neumann, “Internal bias in ferroelectric ceramics: origin and time dependence,” *Ferroelectrics*, vol. 87, no. 1, pp. 109–120, 1988.

[2] G. Arlt and U. Robels, “Aging and fatigue in bulk ferroelectric perovskite ceramics,” *Integr. Ferroelectr.*,

vol. 3, no. 4, pp. 343–349, 1993.

[3] S. Steiner, I. Seo, P. Ren, M. Li, D. J. Keeble, and T. Frömling, "The effect of Fe-acceptor doping on the electrical properties of $Na_{1/2}Bi_{1/2}TiO_3$ and 0.94 ($Na_{1/2}Bi_{1/2}$) $TiO_{3-0.06}$ $BaTiO_3$," *J. Am. Ceram. Soc.*, vol. 102, no. 9, pp. 5295–5304, 2019.

[4] M. M. Ismail, A. Ahmed, W. Q. Cao, L. Anjo, and M. Hashim, "Energy storage density of $(Bi_{0.5}Na_{0.5})_{1-x}Sr_xTiO_3$ ferroelectric ceramics under relaxor phenomena," *Appl. Phys. A*, vol. 127, no. 9, p. 675, 2021.

[5] M. Li, H. Zhang, S. N. Cook, L. Li, J. A. Kilner, I. M. Reaney, *et al.*, "Dramatic influence of A-site nonstoichiometry on the electrical conductivity and conduction mechanisms in the perovskite oxide $Na_{0.5}Bi_{0.5}TiO_3$," *Chem. Mater.*, vol. 27, no. 2, pp. 629–634, 2015.

[6] L. Koch, S. Steiner, K.-C. Meyer, I.-T. Seo, K. Albe, and T. Frömling, "Ionic conductivity of acceptor doped sodium bismuth titanate: influence of dopants, phase transitions and defect associates," *J. Mater. Chem. C*, vol. 5, no. 35, pp. 8958–8965, 2017.

[7] F. Yang, P. Wu, and D. C. Sinclair, "Enhanced bulk conductivity of A-site divalent acceptor-doped non-stoichiometric sodium bismuth titanate," *Solid State Ionics*, vol. 299, pp. 38–45, 2017.

[8] O. N. Salman, M. M. Ismail, and A. T. Sam, "Photovoltaic Response of Heterojunction Photodiode based on Ba0. 8Sr0. 2TiO3 Nanorod Film," *ECS J. Solid State Sci. Technol.*, vol. 12, no. 6, p. 65001, 2023.

[9] M. Zhong, Q. Feng, C. Yuan, X. Liu, B. Zhu, L. Meng, *et al.*, "Photocurrent density and electrical properties of $Bi_{0.5}Na_{0.5}TiO_3$-$BaNi_{0.5}Nb_{0.5}O_3$ ceramics," *J. Adv. Ceram.*, vol. 10, pp. 1119–1128, 2021.

[10] A. Zenkevich, Y. Matveyev, K. Maksimova, R. Gaynutdinov, A. Tolstikhina, and V. Fridkin, "Giant bulk photovoltaic effect in thin ferroelectric $BaTiO_3$ films," *Phys. Rev. B*, vol. 90, no. 16, p. 161409, 2014.

[11] T. Choi, S. Lee, Y. J. Choi, V. Kiryukhin, and S.-W. Cheong, "Switchable ferroelectric diode and photovoltaic effect in $BiFeO_3$," *Science (80-.).*, vol. 324, no. 5923, pp. 63–66, 2009.

[12] M. K. Rajbhar, A. Ashina, E. Ramasamy, S. Mallick, T. N. Rao, and G. Veerappan, "A facile co-precipitation method for synthesis of Zn doped $BaSnO_3$ nanoparticles for photovoltaic application," *Mater. Chem. Phys.*, vol. 258, p. 123939, 2021.

[13] P. K. Panda, "Environmental friendly lead-free piezoelectric materials," *J. Mater. Sci.*, vol. 44, no. 19, pp. 5049–5062, 2009.

[14] J. Rödel, W. Jo, K. T. P. Seifert, E. Anton, T. Granzow, and D. Damjanovic, "Perspective on the development of lead-free piezoceramics," *J. Am. Ceram. Soc.*, vol. 92, no. 6, pp. 1153–1177, 2009.

[15] H. Nie, G. Wang, and X. Dong, "New Bismuth Sodium Titanate Based Ceramics and Their Applications," *Adv. Ceram. Mater.*, p. 131, 2021.

[16] A. K. Zak, W. H. A. Majid, M. E. Abrishami, R. Yousefi, and R. Parvizi, "Synthesis, magnetic properties and X-ray analysis of $Zn_{0.97}X_{0.03}O$ nanoparticles (X= Mn, Ni, and Co) using Scherrer and size–strain plot methods," *Solid State Sci.*, vol. 14, no. 4, pp. 488–494, 2012.

[17] S. Mustapha, M. M. Ndamitso, A. S. Abdulkareem, J. O. Tijani, D. T. Shuaib, A. K. Mohammed *et al.*, "Comparative study of crystallite size using Williamson-Hall and Debye-Scherrer plots for ZnO nanoparticles," *Adv. Nat. Sci. Nanosci. Nanotechnol.*, vol. 10, no. 4, p. 45013, 2019.

[18] C. S. Devi, G. S. Kumar, and G. Prasad, "Control of ferroelectric phase transition in nano particulate NBT–BT based ceramics," *Mater. Sci. Eng. B*, vol. 178, no. 5, pp. 283–292, 2013.

[19] S. Hajra, S. Sahoo, R. Das, and R. N. P. Choudhary, "Structural, dielectric and impedance characteristics of $(Bi_{0.5}Na_{0.5})TiO_3$-$BaTiO_3$ electronic system," *J. Alloys Compd.*, vol. 750, pp. 507–514, 2018.

[20] S. Singh, A. Kaur, P. Kaur, S. Thakur, and L. Singh, "Structural and optical properties of $LaFeO_3$ doped sodium bismuth titanate nanoparticles," in *AIP Conference Proceedings*, 2020, vol. 2220, no. 1.

[21] A. Franco Jr, P. Banerjee, and P. L. Romanholo, "Effect of composition induced transition in the optical band-gap, dielectric and magnetic properties of Gd doped $Na_{0.5}Bi_{0.5}TiO_3$ complex perovskite," *J. Alloys Compd.*, vol. 764, pp. 122–127, 2018.

[22] D. D. Dung, M. M. Hue, N. Q. Dung, N. X. Duong, L. H. Bac, N. N. Trung, *et al.*, "Design and characterization of a new (1-x)$Na_{1/2}Bi_{1/2}TiO_3$+ x$Bi(Ti_{1/2}Fe_{1/2})O_3$ solid solution," *Vacuum*, vol. 183, p. 109815, 2021.

[23] W. Q. Cao, R. L. Wang, F. L. Zhou, M. M. Ismail, and R. K. Pan, "Enhance luminescence property of Er in $Bi_{0.5}Na_{0.5}TiO_3$ ceramics by gradient permeation method," *Appl. Phys. A*, vol. 123, pp. 1–5, 2017.

[24] R. Selvamani, G. Singh, V. Sathe, and V. S. Tiwari, "Probing Oxygen Defects in $Na_{0.5}Bi_{0.5}TiO_3$ Ferroelectric by Micro-Raman Spectroscopy," *Phys. status solidi*, vol. 255, no. 7, p. 1800002, 2018.

[25] E. Aksel, J. S. Forrester, B. Kowalski, M. Deluca, D. Damjanovic, and J. L. Jones, "Structure and properties of Fe-modified $Na_{0.5}Bi_{0.5}TiO_3$ at ambient and elevated temperature," *Phys. Rev. B*, vol. 85, no. 2, p. 24121, 2012.

[26] D. Rout, K.-S. Moon, S.-J. L. Kang, and I. W. Kim, "Dielectric and Raman scattering studies of phase transitions in the (100− x) $Na_{0.5}Bi_{0.5}TiO_{3-x}SrTiO_3$ system," *J. Appl. Phys.*, vol. 108, no. 8, 2010.

[27] D. Rout, K.-S. Moon, J. Park, and S.-J. L. Kang, "High-temperature X-ray diffraction and Raman scattering studies of Ba-doped $(Na_{0.5}Bi_{0.5})TiO_3$ Pb-free piezoceramics," *Curr. Appl. Phys.*, vol. 13, no. 9, pp. 1988–1994, 2013.

[28] D. D. Dung, N. Q. Dung, N. B. Doan, N. H. Linh, L. H. Bac, N. N. Trung, *et al.*, "Defect-mediated room temperature ferromagnetism in lead-free ferroelectric $Na_{0.5}Bi_{0.5}TiO_3$ materials," *J. Supercond. Nov. Magn.*, vol. 33, pp. 911–920, 2020.

[29] V. Kabra, L. Aamir, and M. M. Malik, "Low cost, p-ZnO/n-Si, rectifying, nano heterojunction diode: Fabrication and electrical characterization," *Beilstein J. Nanotechnol.*, vol. 5, no. 1, pp. 2216–2221, 2014.

[30] Y. Li, C.-Y. Xu, J.-Y. Wang, and L. Zhen, "Photodiode-like behavior and excellent photoresponse of vertical Si/monolayer MoS2 heterostructures," *Sci. Rep.*, vol. 4, no. 1, p. 7186, 2014.

[31] M. Ansari-Rad, Y. Abdi, and E. Arzi, "Reaction order and ideality factor in dye-sensitized nanocrystalline solar cells: A theoretical investigation," *J. Phys. Chem. C*, vol. 116, no. 20, pp. 10867–10872, 2012.

[32] L. M. Peter, "Characterization and modeling of dye-sensitized solar cells," *J. Phys. Chem. C*, vol. 111, no. 18, pp. 6601–6612, 2007.

[33] P. J. Cameron, L. M. Peter, and S. Hore, "How important is the back reaction of electrons via the substrate in dye-sensitized nanocrystalline solar cells?," *J. Phys. Chem. B*, vol. 109, no. 2, pp. 930–936, 2005.

[34] F. Yakuphanoglu, "Photovoltaic properties of hybrid organic/inorganic semiconductor photodiode," *Synth. Met.*, vol. 157, no. 21, pp. 859–862, 2007.

[35] S. N. A. Zaine, N. M. Mohamed, M. Khatani, A. E. Samsudin, and M. U. Shahid, "Trap state and charge recombination in nanocrystalline passivized conductive and photoelectrode interface of dye-sensitized solar cell," *Coatings*, vol. 10, no. 3, p. 284, 2020.